SUPPLEMENTARY INFORMATION:

A Computational Study of Laminar-Flow Secondary Separation on a Slender Delta Wing

Ian P Jones[+] and Norman Riley[*]

Retired Consultant, Formerly of ANSYS UK Ltd.
Wantage, Oxfordshire, UK
ian.jones999@gmail.com

* School Of Mathematics
University of East Anglia: NR4 7TJ, UK
n.riley@uea.ac.uk

ABSTRACT

This document contains supplementary information for a paper to be published in The Aeronautical Journal[1] on a computational study of laminar flow over slender delta wings. The paper concentrated on two cases for which measurement data was available, that of Fink and Taylor[2] and Marsden, Simpson and Rainbird[3]. The agreement with the available data, both for surface pressures and contours of total head was very good. Comparisons were also carried out with the results from vortex sheet models of the flow, Smith[4] and the hybrid vortex sheet / boundary layer model of Kirkkopru and Riley[5].

This document contains additional information for the study focussing on:
- Details of the numerical methodology, including the geometry, meshing, convergence and sensitivity to numerical parameters.
- Further information on the results presented in paper.
- Qualitative results from an additional case for which limited measurement data[6,7] is available.

This information should give confidence in the robustness of the methodology used, and be of interest to those interested in the CFD details.

March 2018

Contents

1. Nomenclature

b	Wing span
C_p	Pressure coefficient $(p-p_\infty) / (1/2 \, \rho \, U^2)$
H	Total head $(p - p_\infty + \frac{1}{2}\rho u^2)/ (1/2\rho U^2)$
L	Root chord
p	Pressure
p_∞	Upstream pressure,
Q	Normalised 2nd invariant of the velocity tensor
Re	Reynolds number $\rho \, U \, L \, / \, \mu$
Re_r	Reynolds number based on local wing semi-span
s	Wing semi-span
u	Local flow speed
U	Upstream flow speed
x,y,z	Spatial coordinates
α	Angles of incidence
γ	Semi-apex angle
μ	Dynamic viscosity
ρ	Density

2. Introduction

Jones and Riley[1] present results from a CFD study for the leading edge vortex flows over a delta wing, focussing on the structure of the secondary flow separation induced by the primary vortex. The paper concentrated on two cases for which measurement data was available, those of Fink and Taylor[2] and Marsden, Simpson and Rainbird[3]. Comparisons were also carried out with the results from vortex sheet models of the flow, Smith[4] and the hybrid vortex sheet / boundary layer models, see Kirkkopru and Riley[5]. The modelling approach was briefly summarised, and the results were compared with flow measurements and with results from vortex sheet methods. The results showed very good agreement with measurements for the surface pressure distribution and the secondary flow structure from contours of the total head, and help to understand the complex structure of leading edge vortex flows.

This document contains additional detailed information for the study focussing on:
- Geometry and Meshing, including the adaptive meshing.
- Sensitivity of the results, especially to the mesh structure and the modelling details.
- Further flow visualisations not included in the paper.
- Results for an additional case study for a configuration for which measurement data, Liu et al[6] and Wooding and Liu,[7] is available. Qualitative comparisons of the CFD results with their measurements of skin friction lines and 2D streamlines of sections show that the CFD is able to reproduce key features of the data.

This information provided should give increased confidence in the robustness of the methodology used, be of interest to practitioners of CFD, and give further information on the structure of leading edge vortex flows.

3. Geometry and Meshing

A schematic representation of the geometry and notation is given in Figure 1.

The wing is enclosed in a rectangular domain whose walls are sufficiently far enough away so as not to influence the results. The origin of the computational model was located on the symmetry plane Symmetry was assumed in the model, with the (y.z) plane as a symmetry plane at x=0, so that only half of the geometry needed to be modelled, cutting down on the number of mesh points required, The suction surface of the wing is aligned with the (x,y) plane, with the origin at the trailing edge. To achieve the desired angle of incidence the flow is inclined at an angle α upwards at the inflow face.
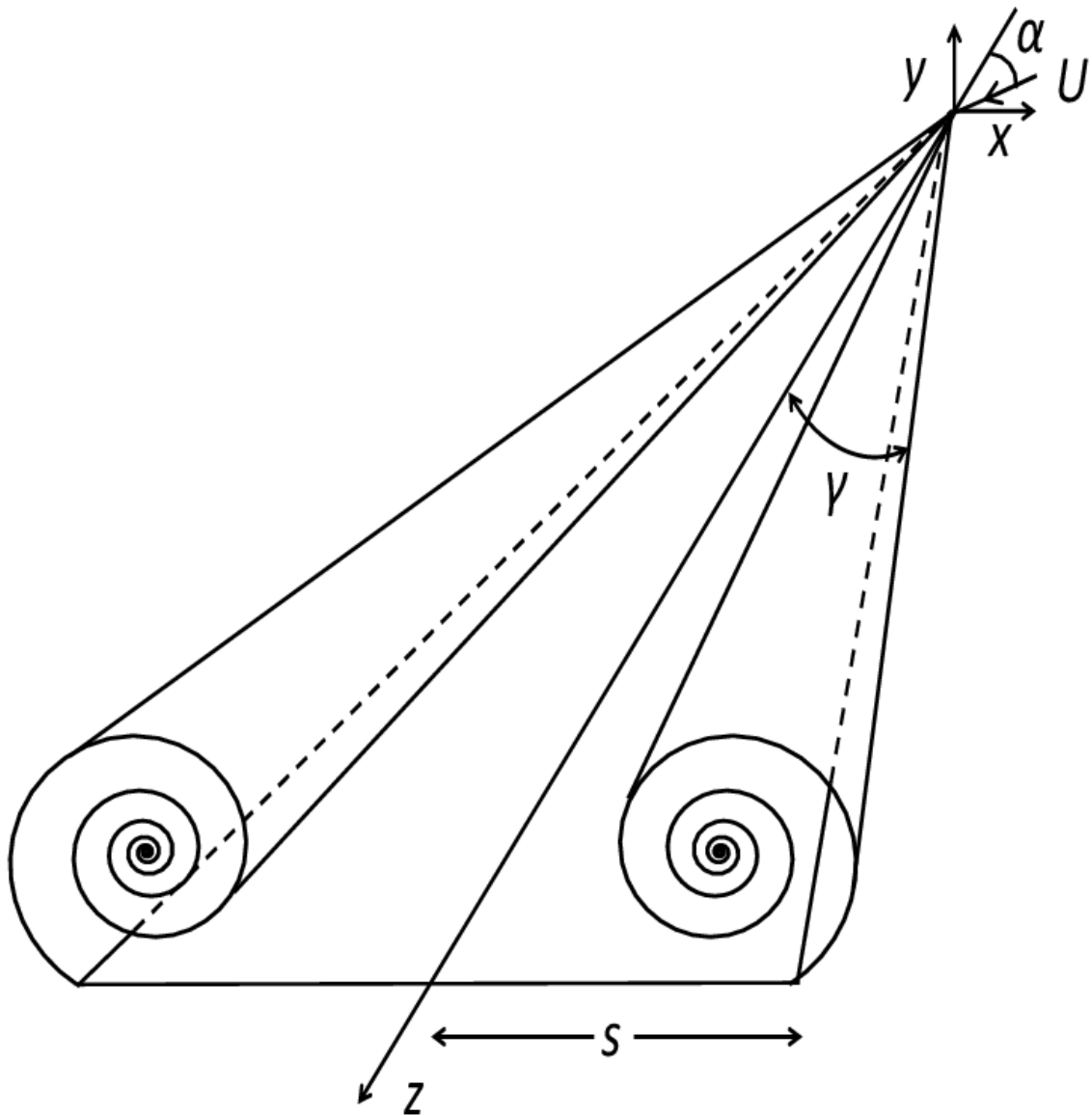
Figure 1: Schematic representation of leading edge vortices.

Details of the operating parameters for the measurements of Fink and Taylor, and Marsden, Simpson and Rainbird are given in Table 1. The comparison with the CFD results focussed on a subset of the measurements, where data on the flow structure was available.

	Fink and Taylor[2]	Marsden, Simpson and Rainbird[3]
Semi-apex angle, γ	10º	20º
Angles of incidence, α	3º, 5º, 10º and 15º (E2 shape) 5 º and 15º (E1 shape)	3.9º, 8.8º, 14º
Root chord	24"	18"
Measuring section	11.28"	12" for the total head measurements.
Flow speed U	80 ft/sec	130 ft/sec. The simulations were carried out at 13 ft./sec.
Reynolds number based on root chord, Re	9.8E5	1.2E6. 1.2E5 for the CFD model.

Table 1 Geometric and Flow Parameters: Experimental Data

Details of the size of the computational domains used are given in Table 2 below. The three external side surfaces of the domain were treated as 'openings' so that fluid could be entrained into the domain with the inflow speed, or exit from the domain as appropriate, see the ANSYS CFX Manuals[8]

for more details on this boundary condition. Tests carried out indicate that the external boundaries were sufficiently far enough away so as not to materially influence the results.

	Fink and Taylor	Marsden, Simpson and Rainbird
Top Height of Box (y)	0.2797	0.2797
Depth of Box (y)	-0.20151	-0.20155
Inflow (z)	0.746	0.591
Outflow (z)	-0.3847	-0.38479
Outer Side (x)	0.4	0.4
Total Box Length	1.1307	0.975786
Upstream from Apex	0.13442	0.133204
Wing Root Chord	0.61158	0.457796
Wing Width	0.1078	0.166624

Table 2: Dimensions for the Computational Domain. These dimensions are all in metres, and the inflow and outflow distances are from the axis origin on the centre line of the wing at the trailing edge.

3.1 Geometry: Fink and Taylor Configuration

Two slightly different delta wing shapes, E1 and E2, were used by Fink and Taylor. The E1 wing was made from a flat plate 0.128" thickness, with a constant chamfer of ¾ inch on both the upper and lower surfaces, and a finite leading edge of 0.013". This was used for the surface pressure measurements.

The E2 wing had an identical planform and thickness to the E1 wing. The purpose of the E2 wing was to eliminate the possibility of the chamfer triggering the secondary separation. It had a flat upper surface, the suction surface, and a 1.5" chamfer on the other side with a finite leading edge of 0.009" and a chamfer angle of 4¾ degrees. Wing E2 was used for the Total Head measurements. Fink and Taylor noted a stronger secondary separation for Wing E1 and an increased extent for the constant pressure region outboard of the suction peaks for wing E2 but '*in other respects the results were quite comparable with those on wing E1'*.

The geometry used in the simulations had a triangular cross-section, with a flat upper surface (suction side) and a leading-edge angle of around 6°. The same geometry was used for all of the simulations presented in the paper. The geometry used was therefore closer to that for E2.

ANSYS Design Modeler and ANSYS Meshing were used to generate a parametric model for the geometries and meshes used in the study.

3.2 Meshing

Because of the wide variety of length scales in the geometry and the flow, unstructured mixed-element meshing has been used. It is not easy a-priori to get suitable meshes with manual mesh generation, as the structure of the flow is not known. A lot of trial and error experimentation was therefore carried out on the meshing parameters, to have a mesh that resolved the main features of the flow, but was not too large, so that it would run on the available computers. In the boundary layer around the wing, mesh inflation was used, with prismatic (wedge) elements to give a mesh aligned with the near-wall flow. Away from the wing in the bulk of the flow, tetrahedral elements were used. Based on initial flow results which indicated the size of the primary leading edge vortex and boundary layers, mesh controls were applied manually to refine the mesh close to the wing surface and near to the leading edge of the wing, where the flow gradients were largest.

Once a suitable initial mesh was obtained, adaptive meshing was used to selectively refine the mesh further. Gradients of the total pressure were used as the adaption variable. This concentrated the mesh further near to the leading edge of the wing to capture the sharp gradients in this region and in the boundary layer on the wing. It did not concentrate the mesh points appreciably near the vortex sheets as the total head is smooth across a vortex sheet. Further research would be needed to

identify an optimal meshing strategy for problems such as these where there are vortex sheets and wakes whose scale and locations are not known a-priori.

For each case, three adaption steps were used, with a target of doubling the number of mesh nodes from the initial mesh with an adaption criterion of the solution variation of total pressure. The final number of mesh nodes used for each case are given in Tables 3 and 4. Because the variation in α is relatively small for the Marsden et al configuration, the meshing procedure outlines here was applied to $\alpha = 8.8°$ and the same mesh was used for $\alpha = 14°$.

Angle of Incidence α	Number of Grid Nodes
5°	3172096
10°	3133227
15°	3196973

Table 3: Mesh Sizes, Fink and Taylor Configuration

Angle of Incidence α	Number of Grid Nodes
8.8°	2449847
14°	2449847

Table 4: Mesh Sizes, Marsden, Simpson and Rainbird Configuration

As a similar approach has been used for all the meshes used in this study, it is illustrated on the Fink and Taylor configuration with an angle of incidence $\alpha = 10°$. Figure 2 below shows the final adapted mesh on the top surface of the wing, showing the much finer mesh near to the leading edge and apex of the wing.
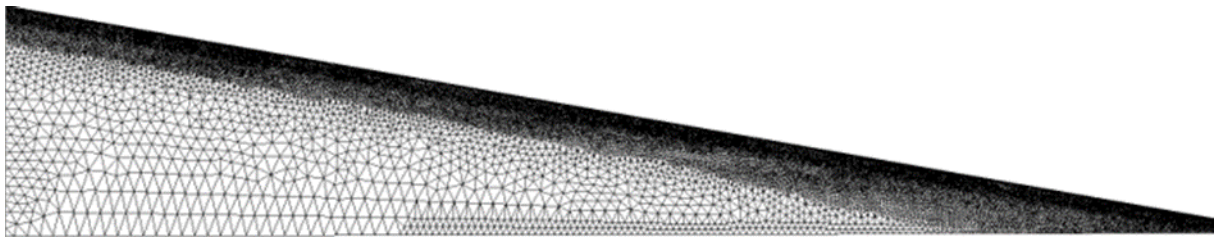
Figure 2: Surface mesh on the top surface (suction side) of the delta wing, viewed from above.

Figure 3 shows a more detailed view of the mesh near to the leading edge, illustrating the very large variation in the mesh sizes used, especially near the leading edge of the wing.
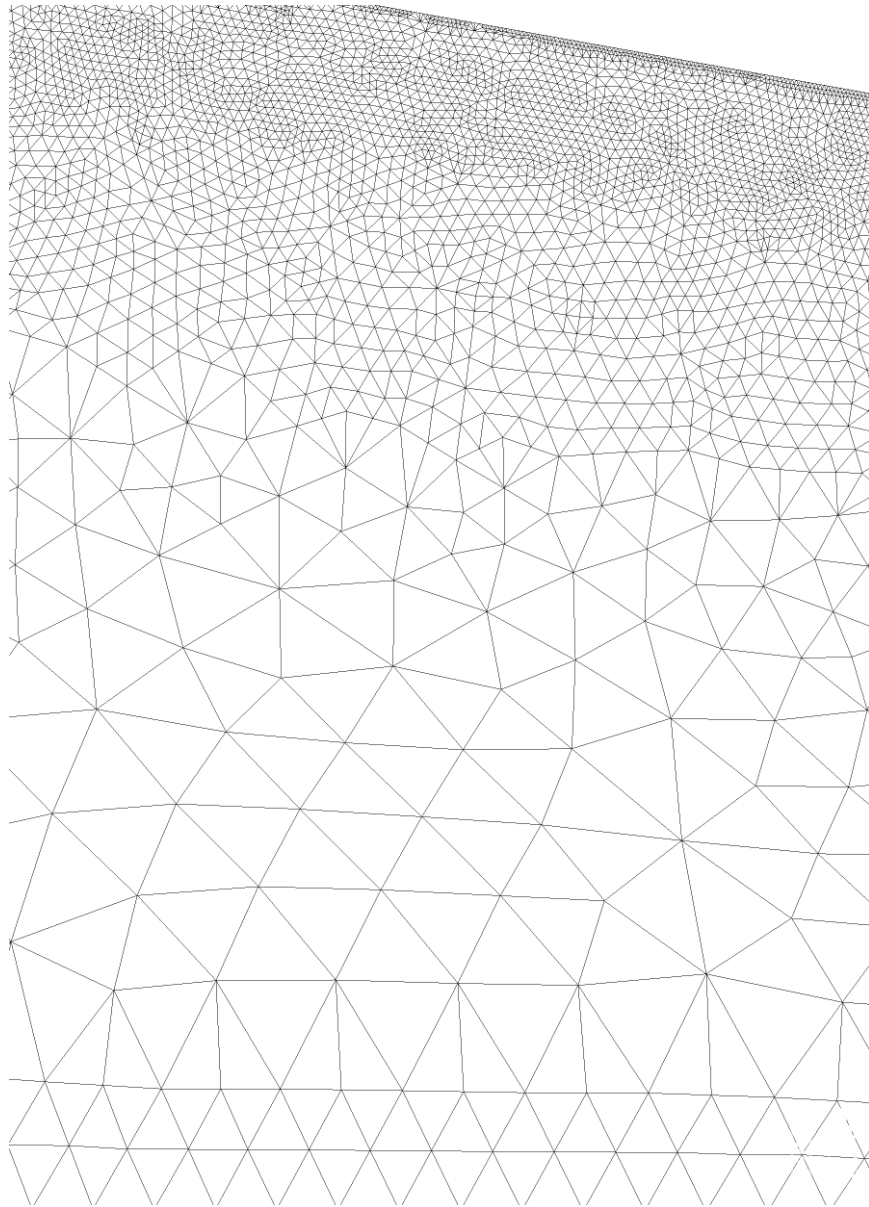
Figure 3: Zoomed in view of the top-surface mesh on the delta wing to show the mesh in the vicinity of the leading edge.

Figure 4 shows the mesh on the symmetry plane, illustrating the prismatic layers near to the wing, and Figure 5 shows a zoomed-in section of the mesh on this plane, near to the wing, showing, the prismatic inflation layer close to the wing surface, with a further subdivision of the mesh, halving the mesh size parallel to the wing, as a result of the adaptive meshing.
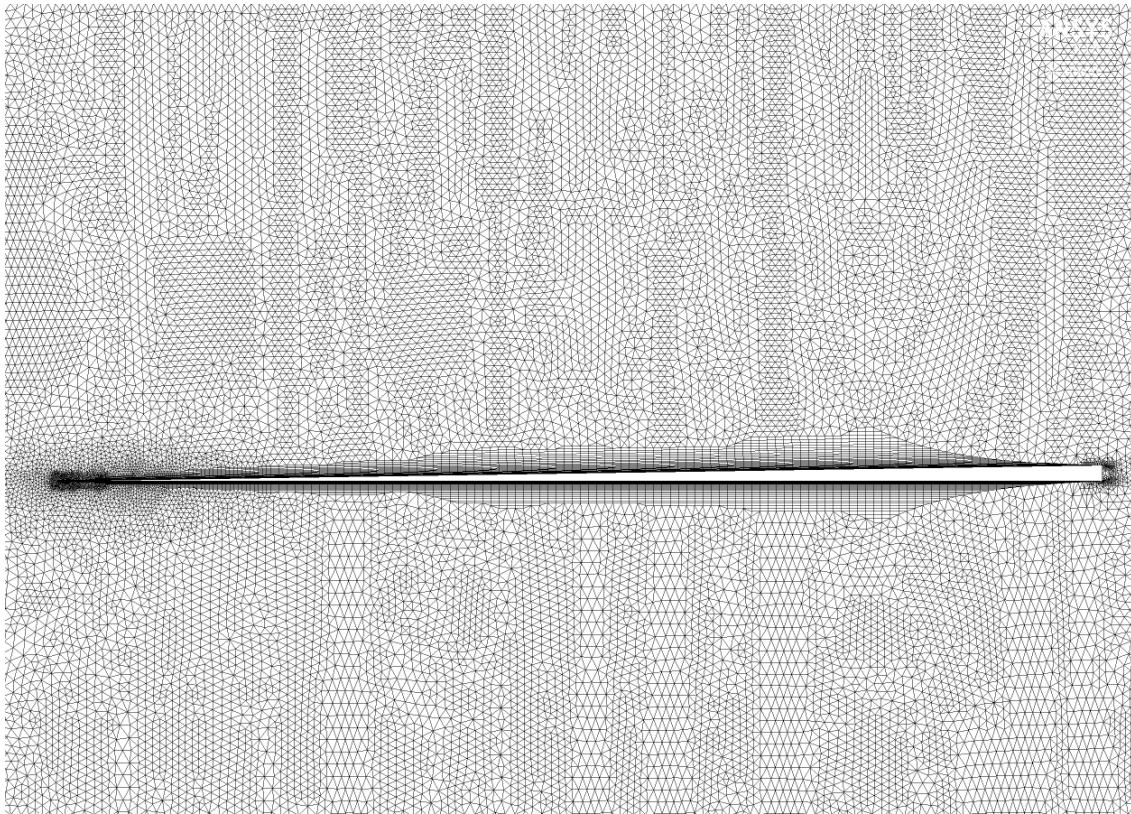
Figure 4: Mesh on the symmetry plane, illustrating the use of an inflated prismatic mesh near the wing surface.
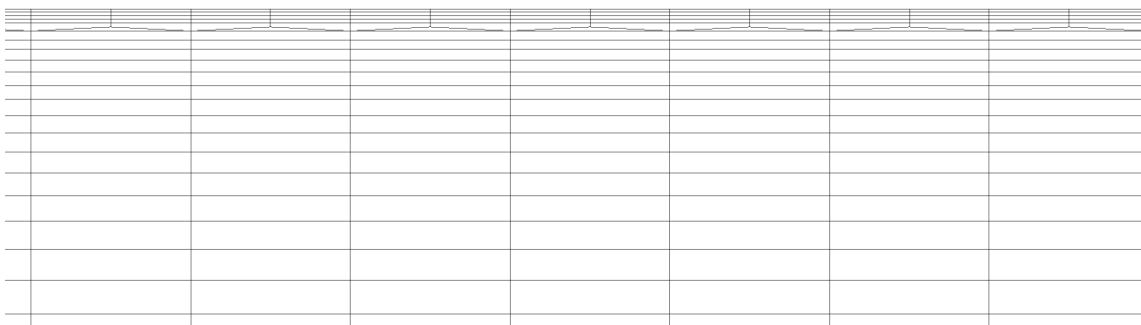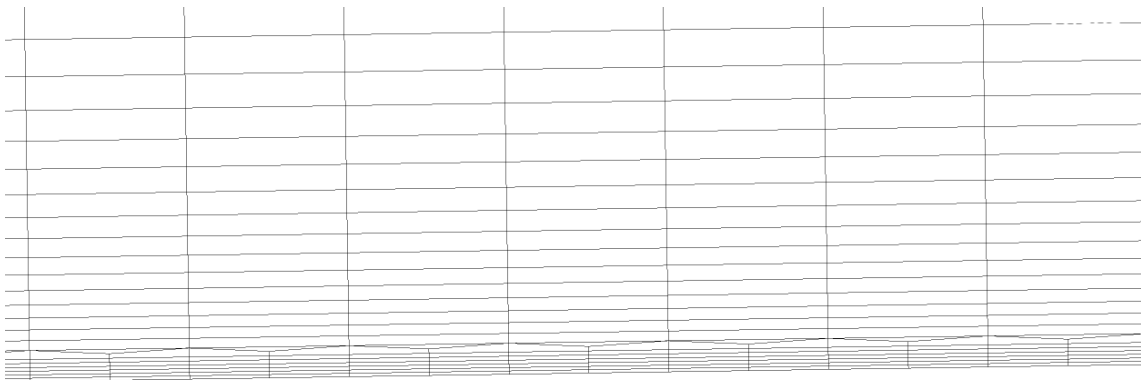
Figure 5: Zoomed in view of the mesh on the symmetry plane.

3.3 Mesh Sensitivity: Effect of Adaption

In order to understand further the sensitivity of the numerical results and the effect of the adaptive meshing on the solution, a numerical solution for the Fink and Taylor case at $\alpha = 10°$ was obtained using the initial unadapted mesh and the results compared with those from the adapted mesh, with approximately double the number of mesh points.

Figure 6a shows a cross-section through the initial mesh used as the basis for the adaptive meshing on the plane where Fink and Taylor presented their measured data. The graticules are the same as those in Figure 3 of Jones and Riley, at 10% of the local wing semi-span. The final mesh, in Figure 6b, shows the way that the adaptive meshing has concentrated the mesh near to the leading edge and the wing surface.

a)   b)
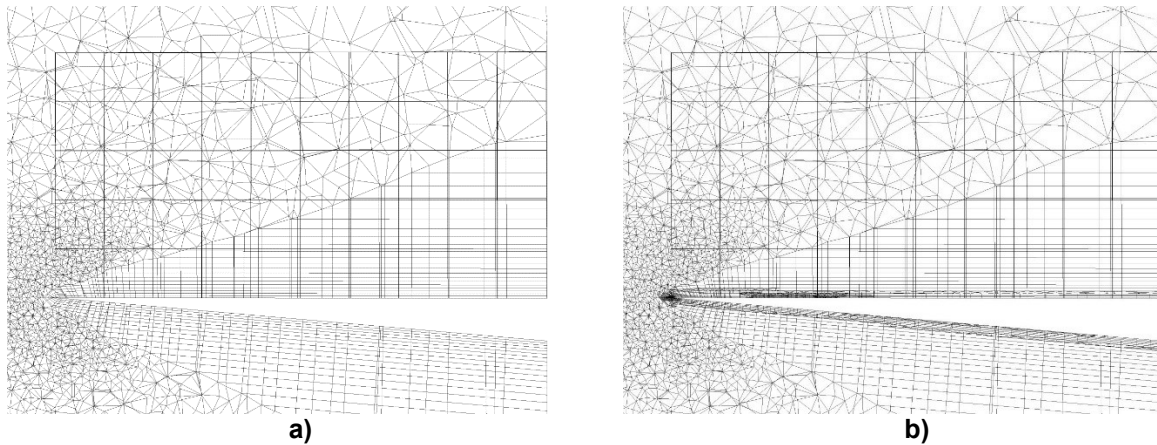
Figure 6: Section of the mesh on the measurement plane a) before adaption b) after adaption.
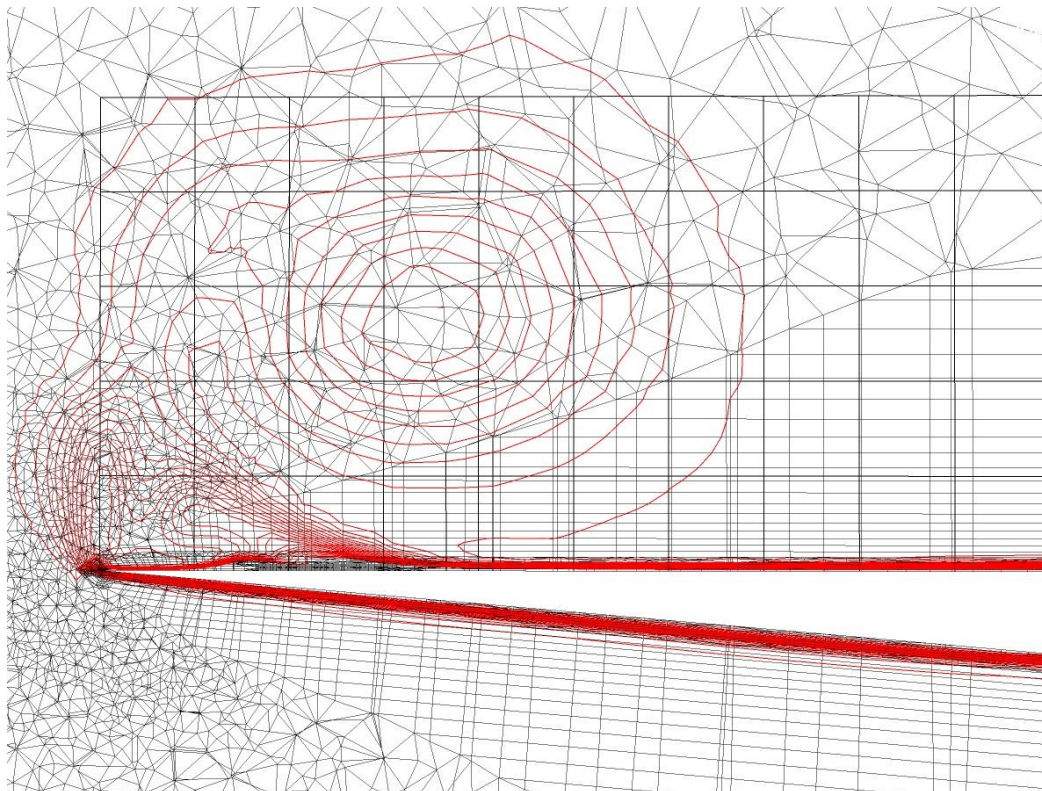
Figure 7: Section of the mesh on the measurement plane, with contours of the total head in red, showing how the mesh refinement has focused on the regions where the contours are densest.

To demonstrate the effect of the adaption of the solution, Figure 7 shows the image of the final mesh with contours of the total head superimposed, illustrating how the adaptive meshing concentrated the

mesh at the trailing edge and in the gradients of the total pressure on the wing surface near the separation point for the secondary separation.

The effect of this on the overall results can be seen in Figure 8 which presents the contours of the total head from the final solution (in black) and the same contours for the solution on the initial mesh (in red) for α = 10º. Figure 8 shows that the adaptive meshing has had little effect on the overall flow structure of the primary and secondary vortices, and both meshes are in good agreement with the data as shown in Figure 3 of Jones and Riley[1] for the solution on the adapted mesh.
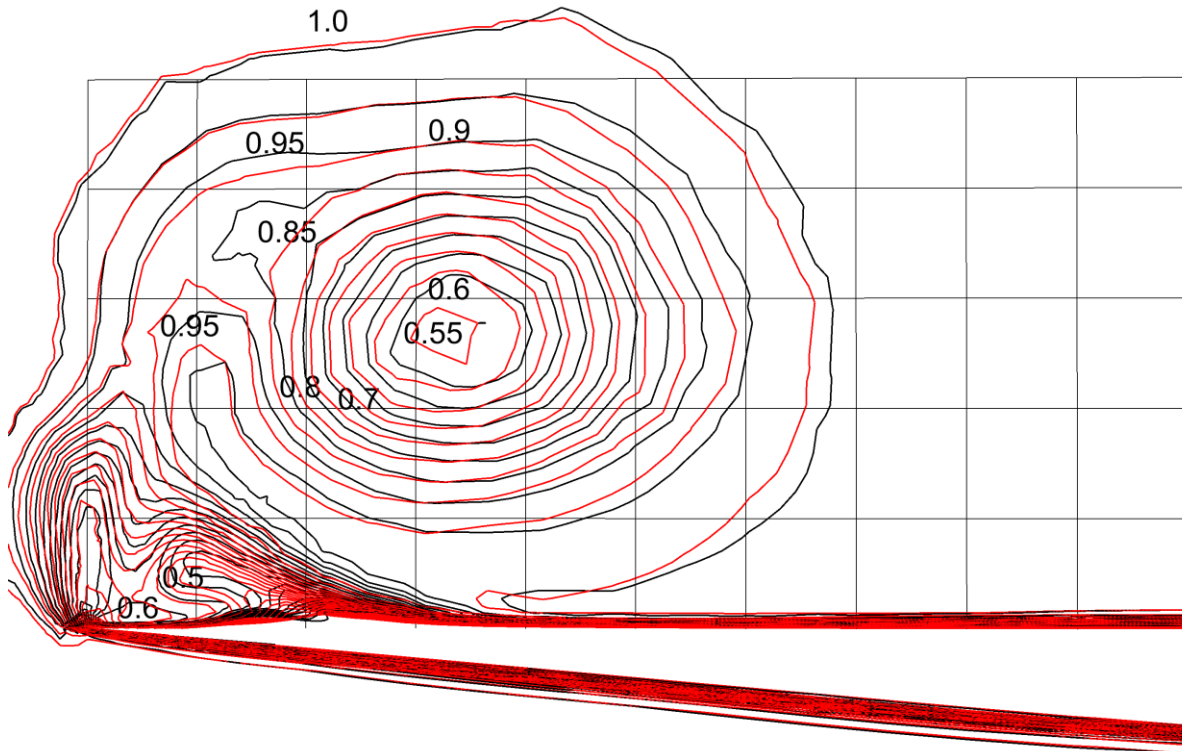
Figure 8. Contours of total head, α = 10º. Black, final adapted mesh, Red initial mesh.

Figure 9 reproduces the plots of pressure coefficient in Figure 5 of Jones and Riley, on which the same result for the unadapted initial mesh for α = 10º has been superimposed. The finer adapted mesh results give a flat profile beneath the leading edge vortex in good agreement with the measured data, whereas the original unadapted mesh has a much rounder profile.
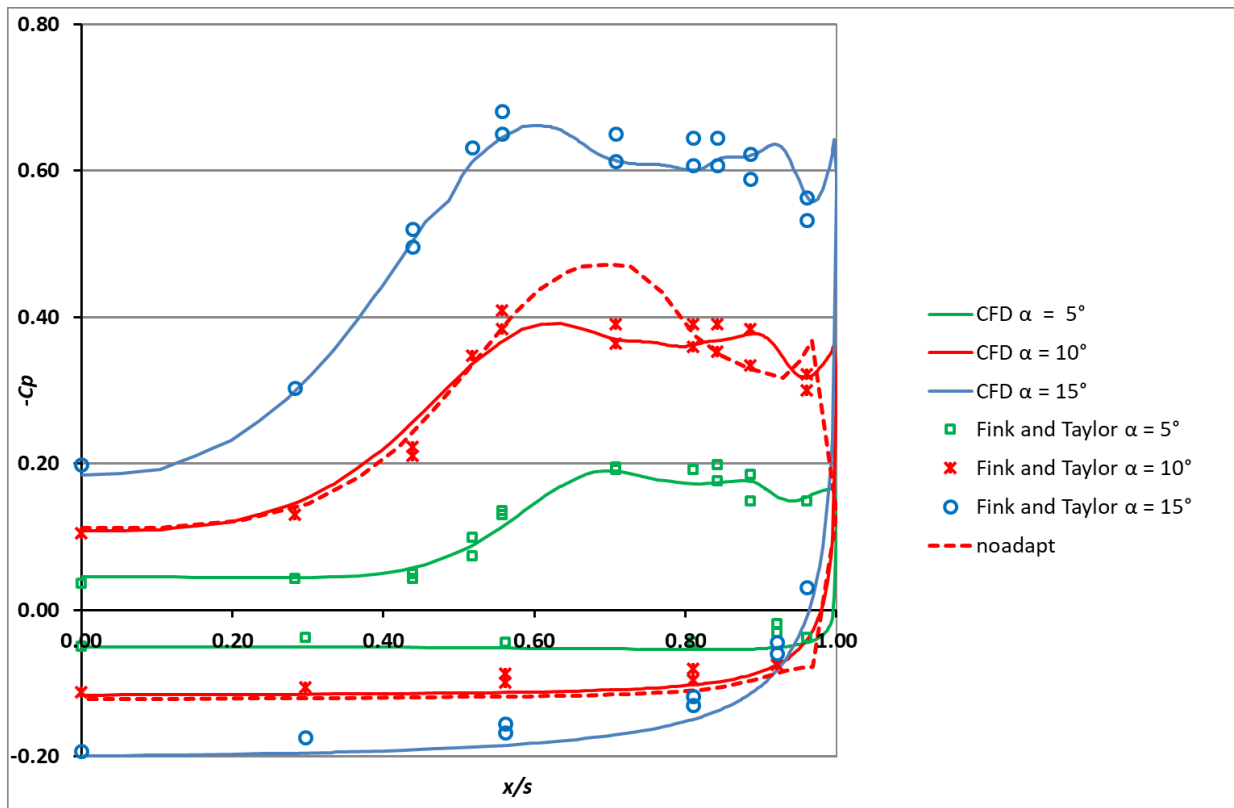
Figure 9: Pressure Coefficients, *-Cp* on upper and lower wing surface for different angles of attack together with results from the initial un-adapted mesh (noadapt) for α = 10º.

3.4 Mesh Sensitivity: Coarse Mesh

In order to increase the confidence in the fidelity of the CFD, a further test was carried out to demonstrate the mesh sensitivity of the results. The additional run was been carried out for the Fink and Taylor test case for α = 10º with a much coarser mesh, with about 1/10 the number of mesh points than that used in Jones and Riley[1]. Figure 10a and 10b reproduce the original results for total head from Figure 3 of Jones and Riley[1], with the measured data and computed results respectively. Figure 10c shows the coarse mesh on this plane compared with the computed result for the coarse grid in Figure 10d. The overall contours look very similar, although the coarse mesh results do not show the details of the secondary flows.
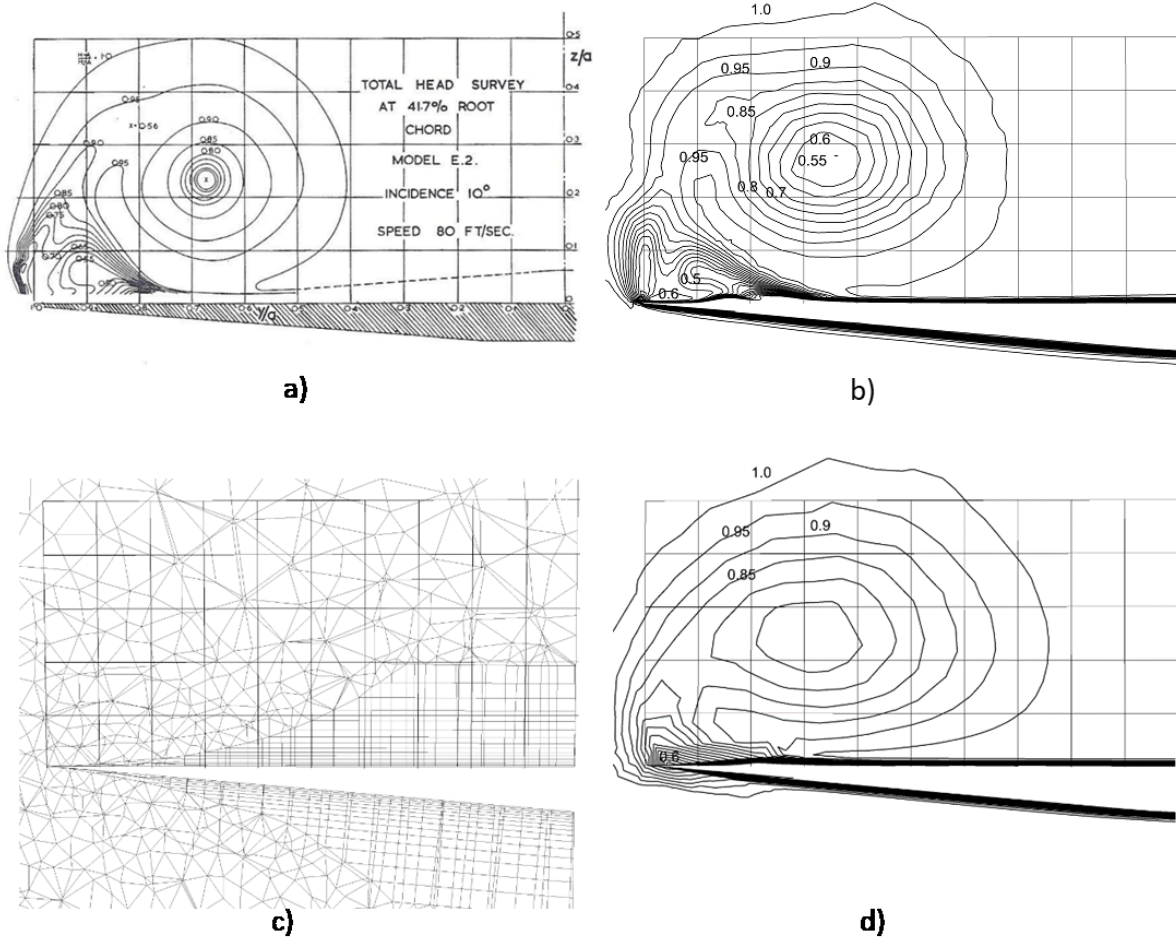
Figure 10: Fink and Taylor case α = 10º. a) Experimental Results for total head, b) fine grid CFD c) coarse mesh d) coarse grid results

Figure 11 plots Cp on the wing surface on the same measurement section. Surprisingly, the results from this coarse mesh show good agreement for the surface pressures, shown in Figure 11, better than the agreement for the unadapted mesh in Figure 9.
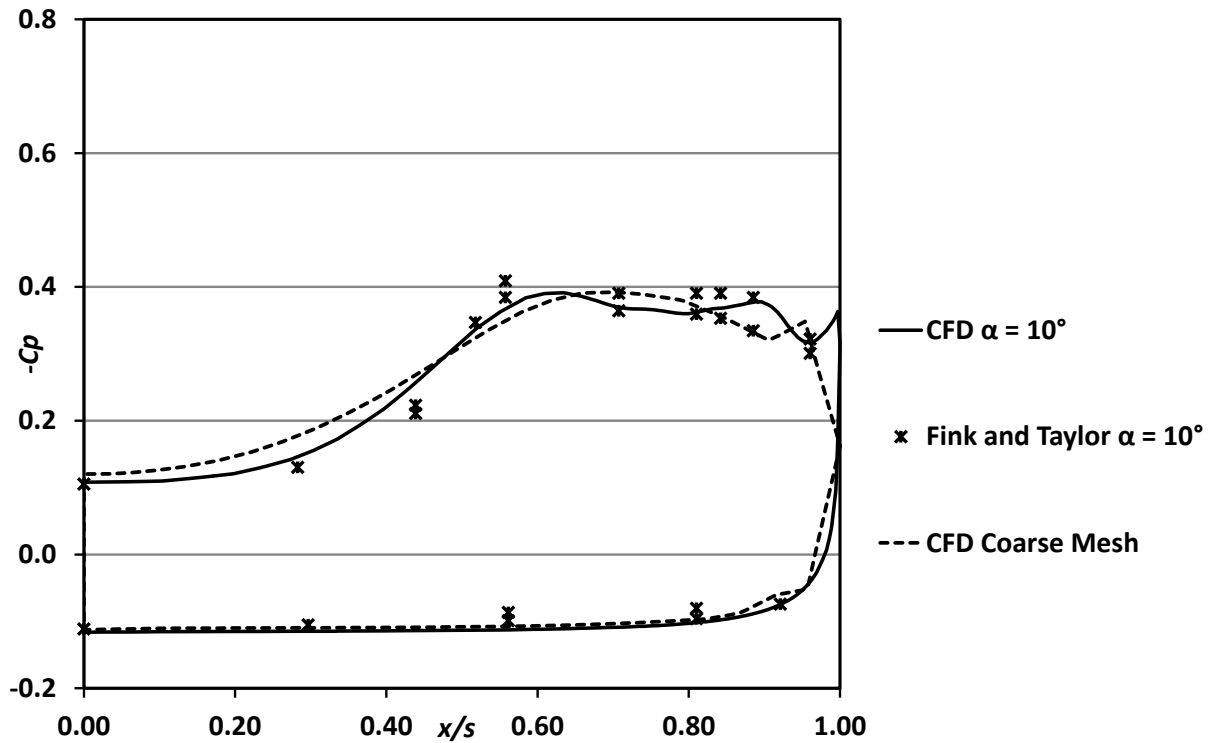
Figure 11: Fink and Taylor Configuration, Cp: Comparison of Fine Mesh results, Coarse Mesh results and the measured data on the wing surface.

Flow visualisations for this configuration with the fine mesh are given in Figure 15 below, showing a lateral instability in the leading edge vortex sheet. Interestingly, this instability did not appear in the coarse grid results.

This mesh sensitivity study has demonstrated the robustness of the results for the meshes used in Jones and Riley[1]. It has also shown that the overall features of the flow can be predicted with much coarser meshes, but that the more refined meshes better predict the detailed small scale features.

4. Comparison with Free Slip Walls

One set of calculations was carried out a zero shear stress (free-slip) boundary condition on the upper and lower surface of the wing, to mimic an inviscid flow without a boundary layer. All other details were exactly the same as for the fine mesh run with a no-slip condition. Figure 12 below shows the contours of Total Head on the same plane as the results shown in Figure 10. There is no sign of the boundary layer and the secondary separation, as to be expected. The centre of the vortex core is slightly below and further outboard that given in Figure 8 for the no-slip condition, as demonstrated in the plots of vortex core location in Figure 14 of Jones and Riley[1].
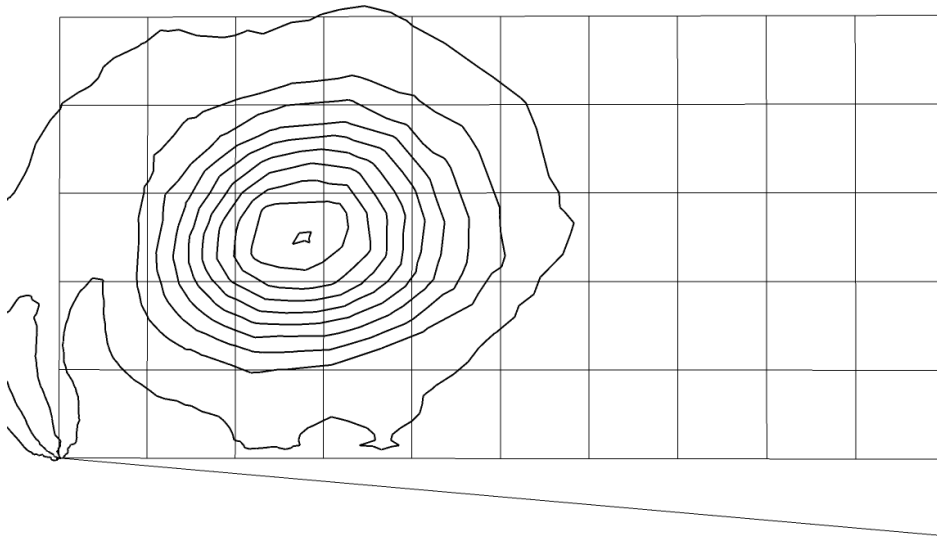
Figure 12: Total Head Contours for a free-slip wall boundary condition.

5. Convergence

As noted in Jones and Riley[1] not all the runs fully converged using the standard convergence criteria for ANSYS CFX. For the Fink and Taylor runs at 5° and 10°, convergence was very good, with the momentum and mass residuals achieving an RMS value of 1.E-5, a factor 10 smaller than the default criteria of 1.E-4. The convergence was slightly less good for α = 15°, but the residuals upstream of the trailing edge were very small, and point values of the solution were steady over the course of many iterations. Note that the convergence was improved slightly by setting the sliver surface at the trailing edge of the wing representing the back face of the wing as a free-slip boundary rather than a no-slip boundary. This simplification does not materially affect the flows upstream of the trailing edge.

For the Marsden, Simpson and Rainbird case, with a larger wing apex angle and at 130 ft./s the runs did not converge, and there were very large fluctuations in point values of the variables. The flow speed in the model was reduced by a factor 10, to 13 ft./s, a Reynolds number of 1.2E5. It still is a large Reynolds number for a laminar flow calculation and it can be expected that there are regions such as near the trailing edge where the flow would be transitional or fully turbulent. Convergence for a laminar flow model would be problematical in these regions. However, for a strongly convective flow such as this, localised disturbances in the region of the trailing edge should not propagate far upstream. In addition, the iterative process used by ANSYS-CFX for steady state problems is a false transient approach, using a local time-step to accelerate convergence. It can therefore be expected that fluctuations in point values of the variables during the iterations are representative of the transient fluctuations that could occur.

The iterations for both angles of incidence for the Marsden, Simpson and Rainbird configuration did not fully converge with an inflow speed of 13 ft./s., with α=14° having larger RMS residuals. Figure 13 shows an iteration (pseudo-time) history of selected point values of the flow velocity components for α=14°. The five points are at 4 locations upstream of the trailing edge near to the vortex sheet, and one in the wake. In increasing distance downstream these are denoted as Points 4,5 6,7 and 8, with Point 4 being the most upstream, and Point 8 in the wake. The figure indicates that over the course of a 100 iterations the fluctuations in the point values are small for the points upstream of the trailing edge, Points 4,5,6 and 7 The fluctuations for these point values are less than 2% of their mean value and less than 2.5% in the wake at Point 8.
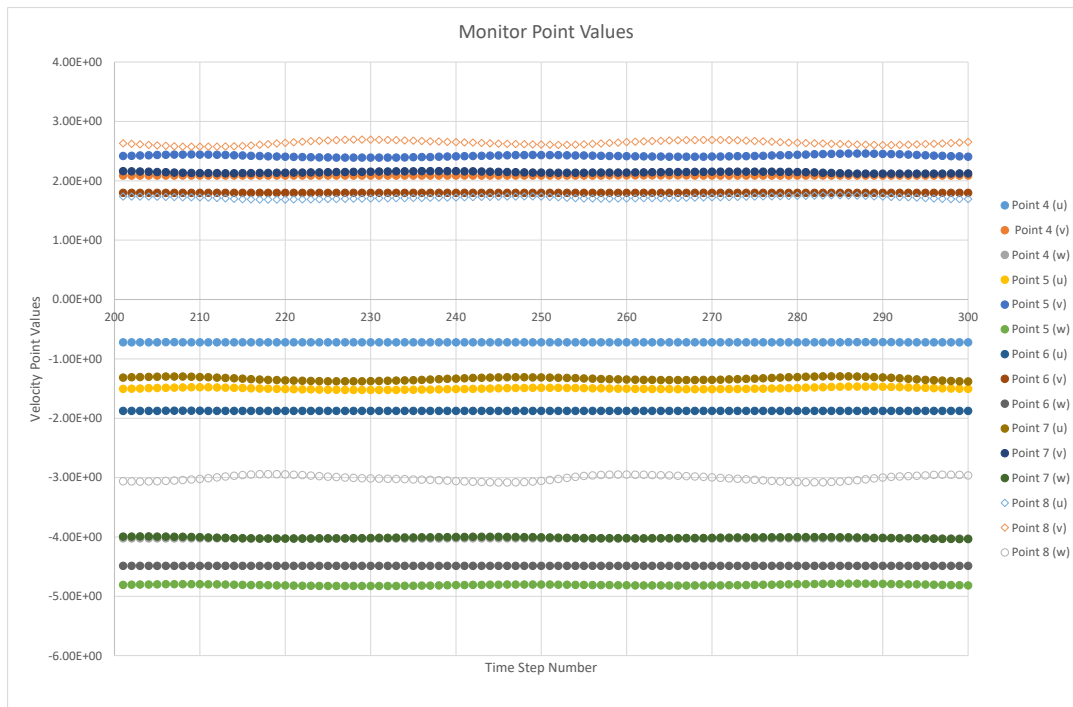
Figure 13: Marsden, Simpson and Rainbird case at α=14°: Time history of monitor point values, at the 5 monitor locations, Points 4-8 increasing downstream with Point 8 in the wake.

The sample locations are shown in Figure 14. Figure 14 also shows the measurement planes, Stations 1-4, along with an isosurface with a value 4E-5 for the average point momentum residual. This demonstrates higher residuals near the trailing edge and in the wake, with only a small amount of propagation upstream. The measurements of the total head were carried out at Station 2, the second plane upstream of the trailing edge. In the volume upstream of Station 2, the residuals have a maximum value of 1.2E-4, with a volume average of 2.9E-8.

These small residual values do demonstrate that while the overall solution has not 'converged' using the standard criterion in the software, the important results at the measurement locations where the comparisons between the results and the measurements were made are very well converged.
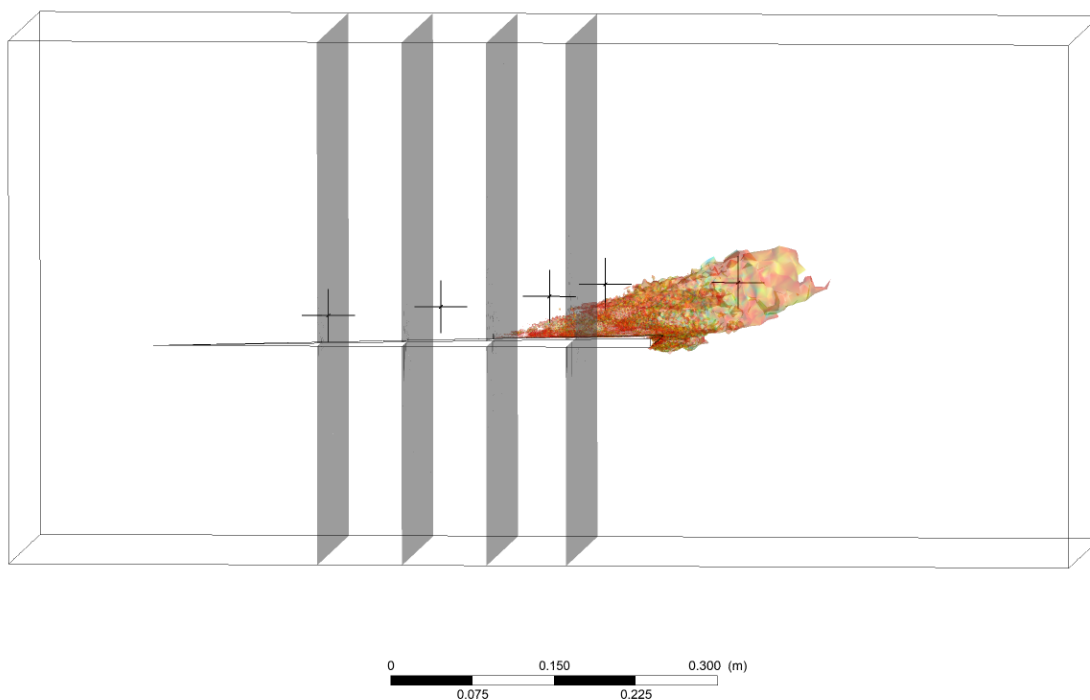
Figure 14: Marsden, Simpson and Rainbird case at α=14°: Isosurface of Residuals at 5.E-5, along with the 4 measurement planes, and the 5 monitor points, points 4-8 from left to right.

6. Further Visualisations.

CFD can generate an enormous amount of visualisation results and it is only possible to present a small subset of these results in the paper[1]. The visualisations in Jones and Riley using vortex cores and streamlines concentrated on the structure of the secondary separation. Additional visualisations are provided here to give further insight into the complex flow phenomena of the leading edge vortex flows, especially the structure of the vortex sheet near the leading edge, and the development of a lateral instability in the leading edge vortex sheet.

6.1 Fink and Taylor, Vortex Core

Vortex cores, plotting an isosurface of a quantity such as 'Q', the second invariant of the velocity gradient tensor can give a good representation of the flow structure. However, with a static 3D image, it can be difficult to see all the structure, because the isosurface can obscure details further away.. The results presented by Jones and Riley for the vortex cores were clipped at the measurement plane with only one viewpoint, to enable the secondary separation to be seen. Figure 15 repeats these plots, but with an additional oblique view, to enable both the secondary separation and the primary vortex sheet to be seen. The reference value of Q, 0.002, has been normalised to give consistent results to other vortex core indicators.
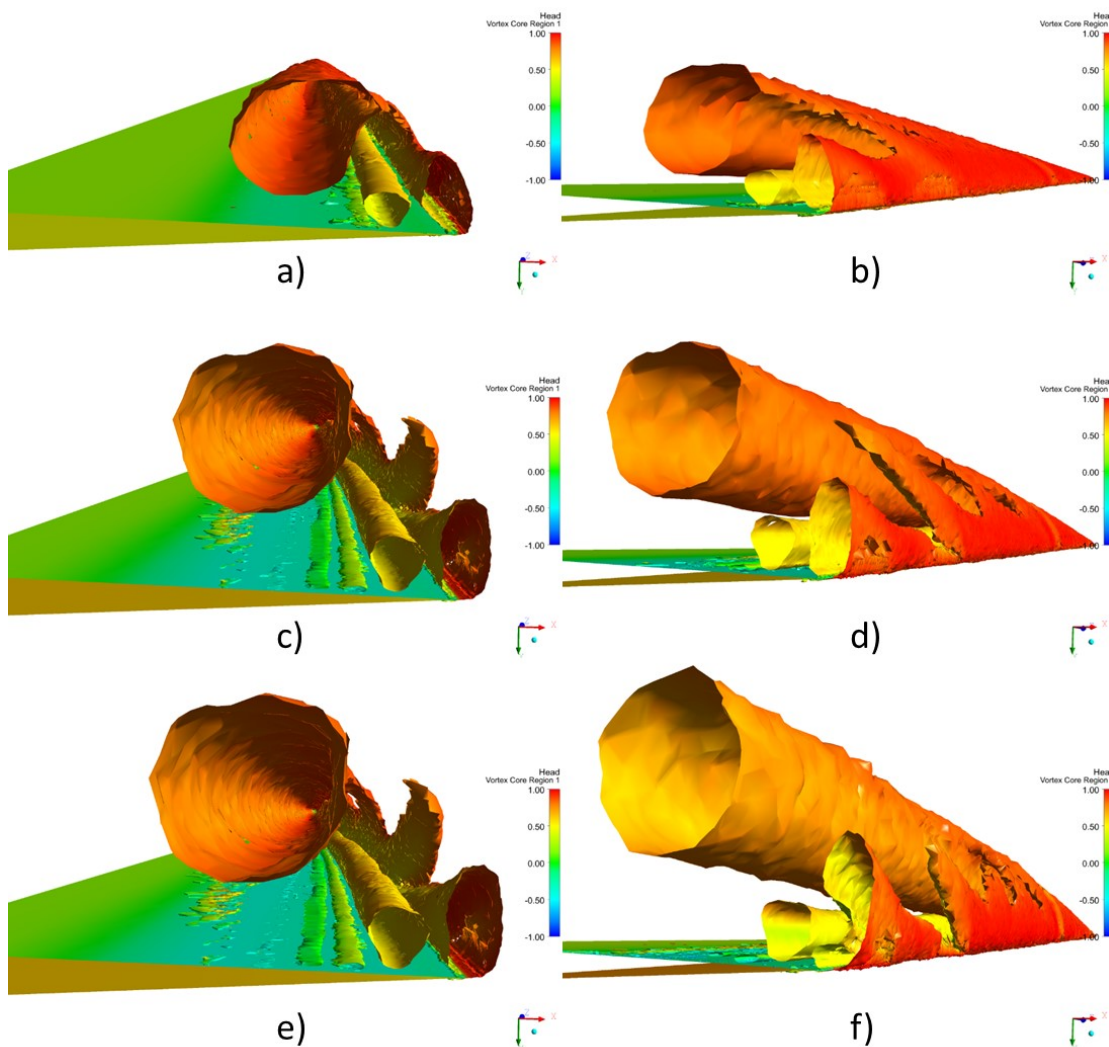
Figure 15: Vortex Cores given by *Q=0.002* , *α = 5°*, a) and b), *α = 10°*, c) and d), *α = 15°*, e) and f). Isosurface coloured by Total Head.

Figure 16 gives a side view of the vortex core, with Q=0.00075 without the clipping of the isosurface at the measurement plane, for α = 10°. This clearly shows the development of the lateral instability of the vortex sheet, the 'fingering'. As noted earlier, this instability is not seen in the computed results using a very coarse mesh.
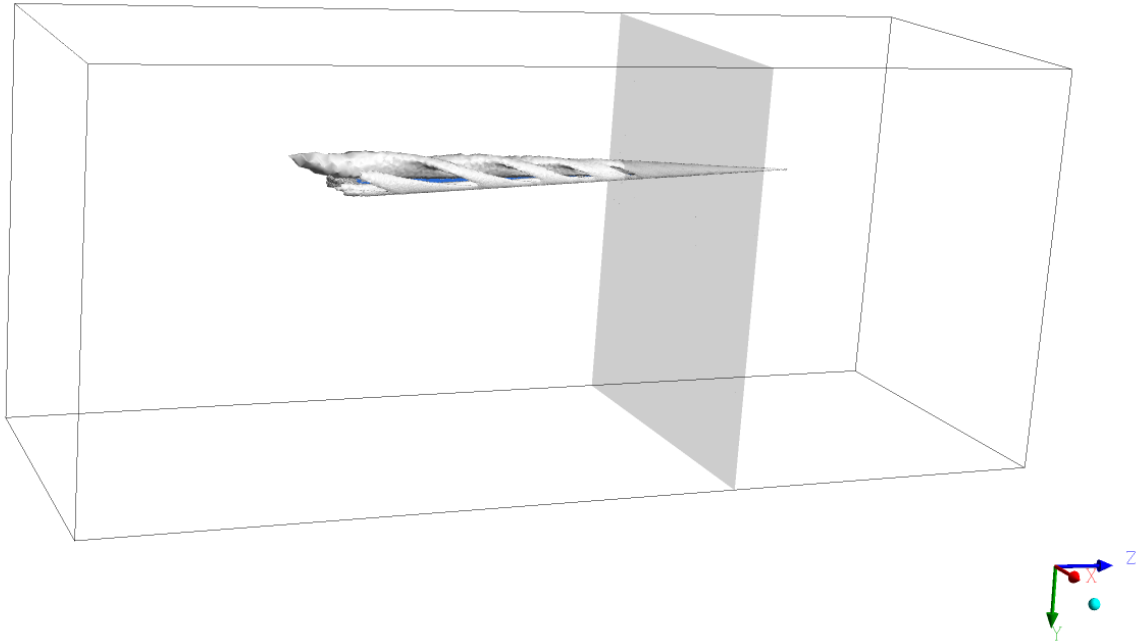
Figure 16: Fink and Taylor configuration, α = 10º: Isosurface of Q, 0.00075 showing the development of the fingering in the primary vortex sheet. The plane shown is the measurement station used to clip the earlier visualisations.

6.2 Marsden, Simpson and Rainbird, Streamlines.

Jones and Riley presented visualisations of the vortex cores for this case, but omitted the streamlines, to reduce the size of the paper. Streamlines for this case are shown in Figure 17. One set of streamlines is released from the leading edge of the wing, coloured by flow speed, and another set from a line inboard of the leading edge, roughly at the location of the secondary separation. This line is shown in red in Figure 17. The purpose of the second set is to highlight the secondary flow structure. To differentiate them from the first set, as with the streamlines for the Fink and Taylor configuration, they are coloured in black. The plots are clipped at Station 2, the measurement station. The results show the same features as the other flow visualisations with the development of the leading edge vortex and the secondary separation near the apex.

For α = 8.8º the secondary separation starts from about the level of the most upstream measuring plane, Station 4, whereas at the higher angle of incidence, the secondary separation starts much further upstream. Further downstream than the onset of the secondary separation, the structure of the primary vortex sheet also appears to change, with a number of the streamlines being entrained by the shear-driven recirculation along the leading edge, rather than into the primary vortex core. The streamlines again indicate that there may be a tendency for the streamlines to concentrate together in ropes, although numerical artefacts cannot be completely ruled out.

| a) | b) |
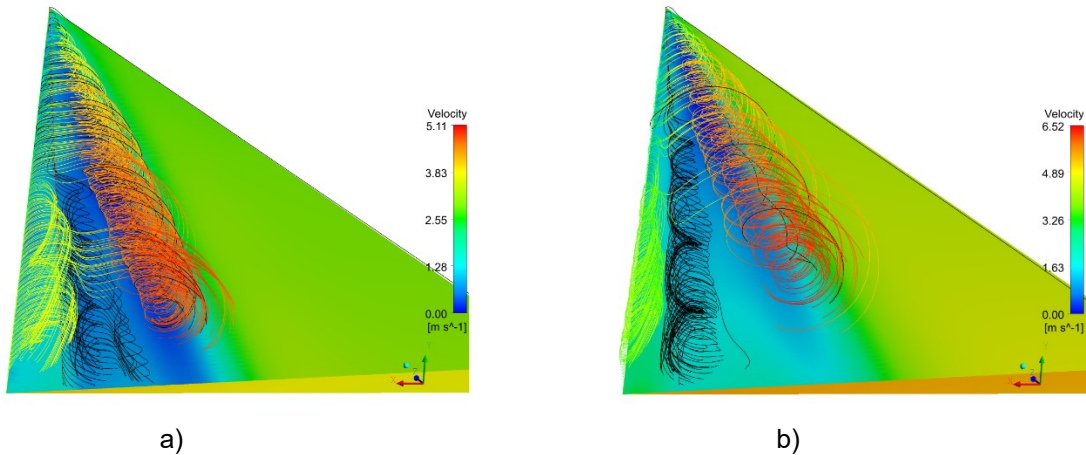
Figure 17: Streamlines, with the view clipped at Station 2: a) α = 8.8º, b) α = 14º.

7. Additional Case Study: Liu et al

Many other authors have presented measurements for leading edge vortex flows over delta wings. This study has concentrated on laminar-flow cases where measurements of the flow structure of the secondary separation are available, as contours of the total head. In the course of this work, other measurements studies have been examined, to provide qualitative information in support of this work. Liu et at [6], and Woodinga and Liu et al[7] have investigated the flow over a 65° delta wing at a Reynolds number based on root chord of 4.1E4[6] in a water tunnel and in air at 4.4E5 [7].The objective of their investigations was to demonstrate techniques for extraction of skin friction fields, from surface luminescent dye visualizations in water and Global Luminescent Oil Film (GLOF) in air. These skin friction fields can be used to help identify the topological structure of the flow fields. They also presented some results from Particle Image Velocimetry (PIV) in air. The skin-friction plots in water presented by Liu et al were consistent with the GLOF measurements and with the PIV results. However, their PIV measurements could not be used for the assessment of secondary flow structures because of a significant amount of 'jitter' in their results.

A CFD model of the Liu et al configuration in water was developed, using the methodology described previously for the other CFD results. The parameters for this case are given in Table 5.

Parameters	Liu
Semi Apex Angle, γ	25º
Angles of incidence, α	10º
Root chord	0.2m
Base Span	0.188 m
Flow speed U	0.175 m/s
Reynolds number based on root chord, Re	4.1 E4
Operating Fluid	Water
Density	997 kg m^-3
Dynamic Viscosity	8.899E-4 Kg m^-1 s^-1

Table 5: Geometric and Flow Parameters, Experimental Data: Liu et al Configuration

Figure 18 compares results for the skin friction fields between the GLOF measurements in air and the CFD model. The topological structures are very similar, demonstrating the Primary Attachment Lines (PAL), Secondary Separation Lines (SSL) and the Secondary Attachment Lines (SAL). The skin-friction fields are qualitatively very similar although in the calculations the attachment and separation lines are further inboard than in the measurements.
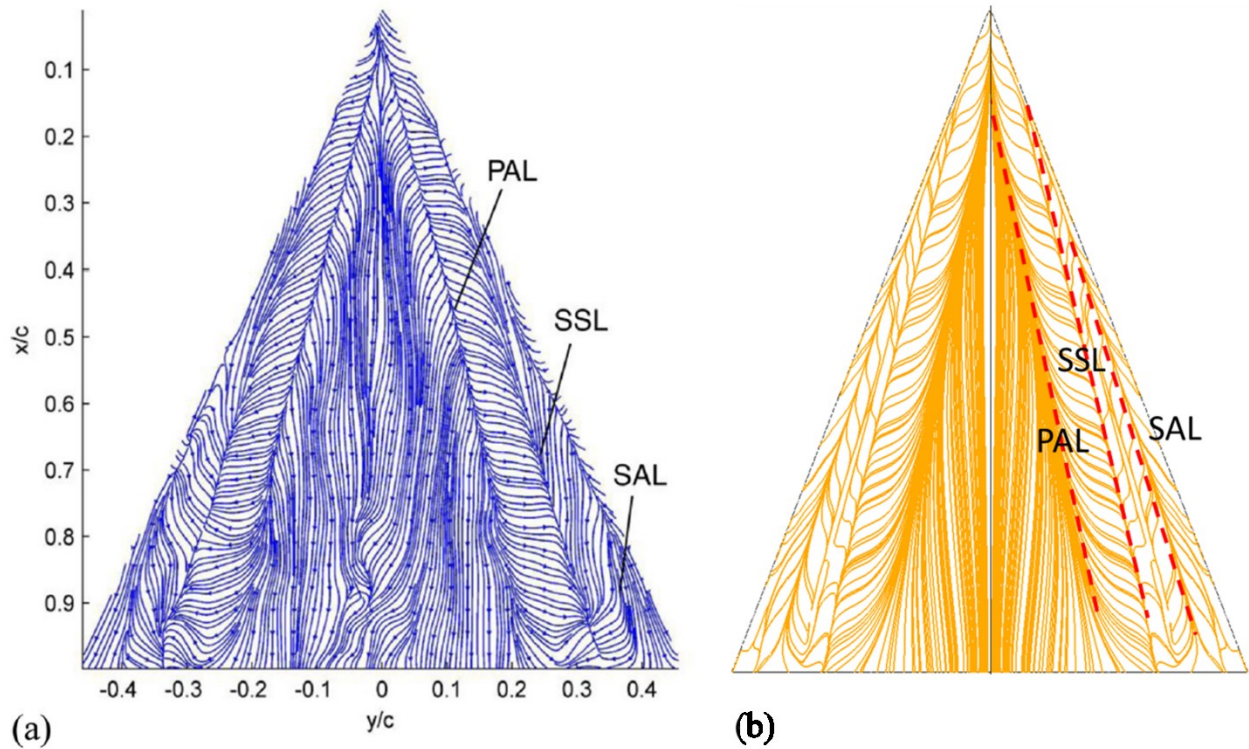
Figure 18: Comparison between skin friction fields using GLOF[6] (a) and the CFD model (b), showing the Primary Attachment Lines (PAL), Secondary Separation Lines (SSL) and Secondary Attachment Lines (SAL).

Liu et al also presented instantaneous snapshots of 2-D streamlines from the PIV on several cross-flow planes. From their results they noted that the centres of the primary leading-edge vortices at different cross-sections remained invariant in their normalized coordinates at $(x,y)/b = (0.33,0.05)$, or $(x,y)/s = (0.66, 0.1)$. They also estimated the secondary separation was induced in the range $x/b = 0.35$ to 0.43, 70% to 83% of wing semi-span, with considerable drift (jitter) within this range.
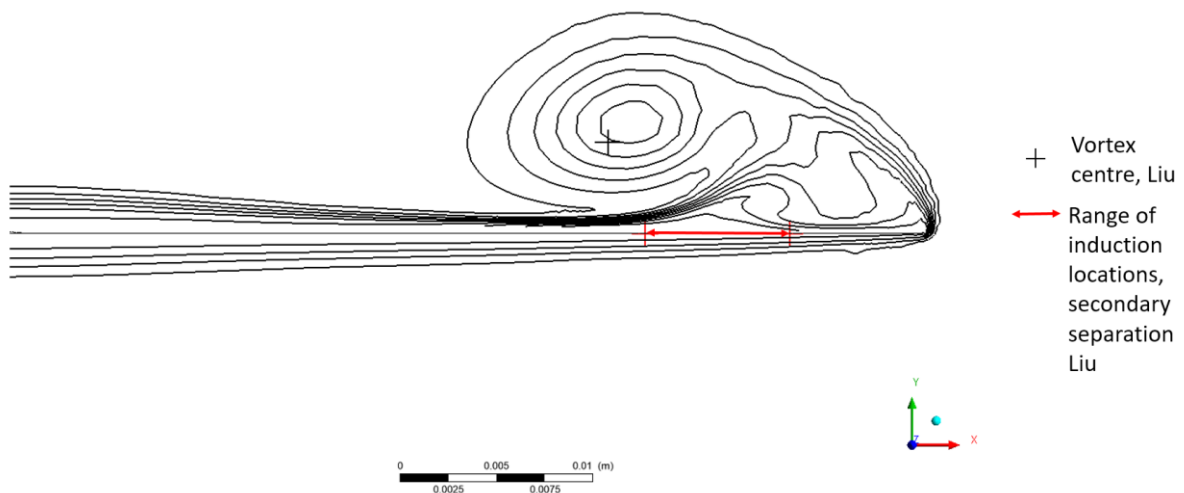
Figure 19: Contours of Total Pressure at z/L = 0.5, along with estimated locations of the vortex centre and induction of the secondary separation.

Figure 19 shows contours of Total Pressure from the CFD on a plane at mid chord z/L=0.5, along with the estimated centre of the vortex core and the range of induction of the secondary separation deduced from the PIV. The vortex centre is slightly lower and more inboard than the CFD, but both

the vortex core location, and the region of the induction of the secondary separation are broadly consistent with the current calculations.
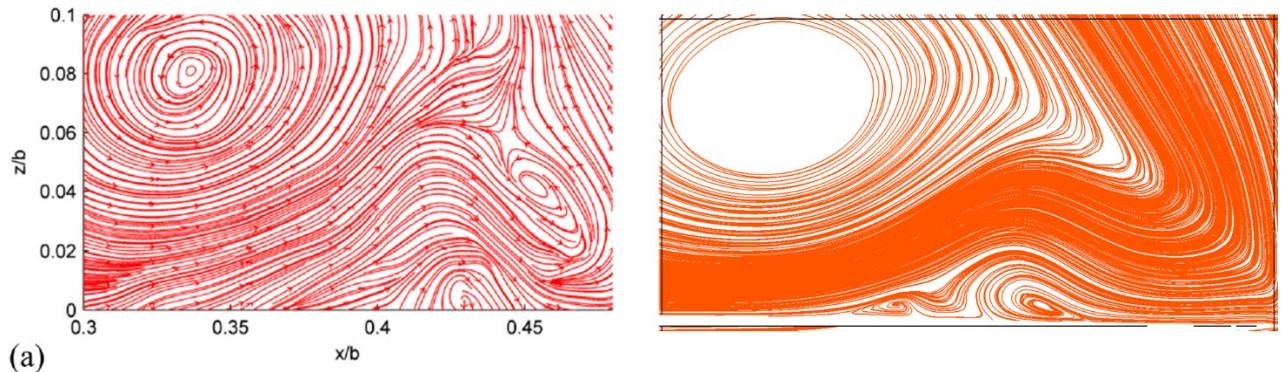
Figure 20: 2D streamlines on a plane at z/L=0.6 a) PIV, b) CFD.
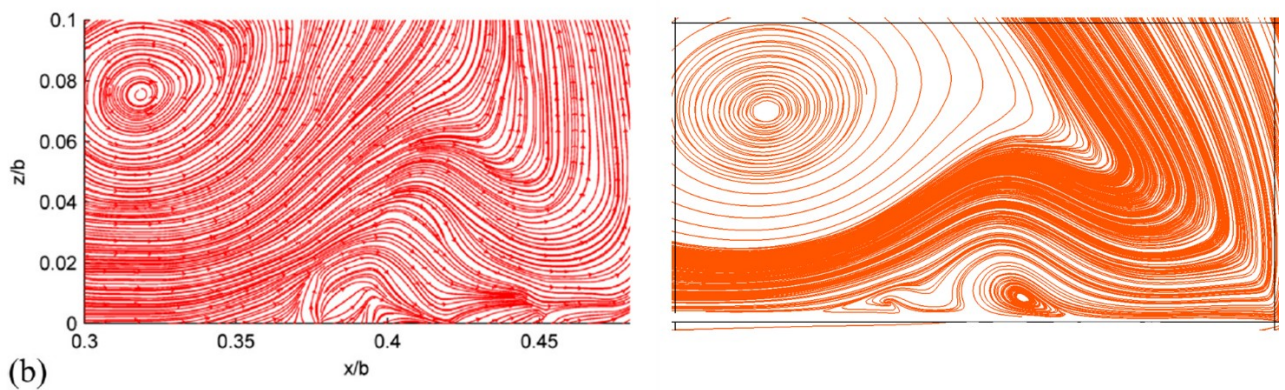
Figure 21 2D streamlines on a plane at z/L=0.72 a) PIV, b) CFD

Figure 20 shows a comparison between 2D surface streamlines obtained from a snapshot of the PIV measurements, and the CFD, at z/L=0.6, and the corresponding results for z/L= 0.72 in Figure 21. The overall shapes of the streamlines are very similar with the streamlines under the primary vortex sweeping upwards over the secondary separation, and then being entrained into the primary vortex sheet. The measured vortex centres are slightly higher than their estimate of z/b= 0.05 shown in Figure 12, and with the vortex centre from the CFD. Figure 20 also shows an additional recirculation in the shear layer between the primary flow and the leading edge. This is neither present in Figure 21 or in the CFD. However, similar structures were present in the computational results presented in the main paper. This recirculation may also be associated with the considerable jitter in the PIV results of Liu et al.

8. Concluding Remarks

The aim of this document has been to provide detailed information on the CFD methodology used by Jones and Riley[1] for the secondary flows induced by the primary leading edge vortex, so as to give increased confidence in the conclusions of that paper. The results presented here have demonstrated the robustness of the results, including mesh sensitivity and convergence. They also highlight a lateral instability in the vortex sheet, observed also in the smoke visualisations of Lowson[9].

In addition, the results for an additional case, that of Liu and co-workers show that the CFD is able to reproduce well the features of their measurements of skin friction fields. Their PIV measurements of the flow field are affected by jitter in the measurements. The cause of this jitter is not known, but it makes it difficult to compare their results with the CFD model. However, the limited comparison carried out between snapshots from their PIV measurements and the CFD results show very similar features.

9. References

1. Jones, I P and Riley, N, A Computational Study of Laminar-Flow Secondary Separation on a Slender Delta Wing, submitted to Aeronautical Journal.
2. Fink, P.T. and Taylor, J., Some Early Experiments on Vortex Separation, Part II. - Some Low Speed Experiments with 20 deg. Delta Wings, ARC R&M 3489, 1955, HMSO. Available from http://naca.central.cranfield.ac.uk/reports/arc/rm/3489.pdf, accessed 16 March 2017.
3. Marsden, D.J., Simpson R.W. and Rainbird W.J., The Flow over Delta Wings at Low Speeds with Leading Edge Separation, *Cranfield College of Aeronautics Report 114*, 1957. Available from http://dspace.lib.cranfield.ac.uk/handle/1826/4081 accessed 16 March 2017.
4. Smith, J.H.B., Improved Calculations of Leading-Edge Separation from Slender Delta Wings, *RAE Technical Report 66070, Proc. Roy. Soc. A* **306**, 1968.
5. Kirkkopru K. and Riley N., Secondary Separation from a Slender Wing, *Journal of Engineering Mathematics*, **25**, 1991, pp 329-352.
6. Tianshu Liu M. H. M. Makhmalbaf RS, Vewen Ramasamy S. Kode P. Skin Friction Fields and Surface Dye Patterns on Delta Wings in Water Flows, J Fluids Engineering, 2015: 137(7) July 2015 DOI: 10.1115/1.4030041
7. Sudesh Woodinga, Tianshu Liu, Skin friction fields on delta wings, Experiments in Fluids, 47:897-911, DOI 10.1007/s00348-009-0686-6, December 2009.
8. ANSYS CFX Manuals, Ansys Inc.
9. Lowson, M.V., Vizualisation Measurements of Vortex Flows. AIAA-89-0191, 27th Aerospace Sciences Meeting, Reno, Nevada, 1989

Table of Figures